

Robust Optimized Pulse Schemes for Atomic Fountain Interferometry

Michael H. Goerz, Vladimir S. Malinovsky*

DEVCOM Army Research Laboratory, Adelphi, MD 20783, USA.

* Correspondence: vladimir.s.malinovsky.civ@army.mil

Abstract: The robustness of an atomic fountain interferometer with respect to variations in the initial velocity of the atoms and deviations from the optimal pulse amplitude is examined. We numerically simulate the dynamics of an interferometer in momentum space with a maximum separation of $20\hbar k$ and map out the expected signal contrast depending on the variance of the initial velocity distribution and the value of the laser field amplitude. We show that an excitation scheme based on rapid adiabatic passage significantly enhances the expected signal contrast compared to the commonly used scheme consisting of a series of Rabi pulses. We demonstrate further substantial increase of the robustness by using optimal control theory to identify splitting and swapping pulses that perform well on an ensemble average of pulse amplitudes and velocities. Our results demonstrate the ability of optimal control to significantly enhance future implementations of atomic fountain interferometry.

1. Introduction

Atom interferometry [1–3] is a core technology for quantum metrology and quantum sensing [4]. Their operating principle exploits the wave nature of matter in the same way that classical optical interferometers exploit the wave nature of light. An initial wavepacket is split into two pathways that are separated spatially. These pathways are then mirrored and recombined. The recombination maps an accumulated phase difference between the two pathways into population at the output ports as an interference pattern.

Since atoms have mass, this relative phase is affected by gravitational fields and accelerations. This enables not only applications in fundamental physics [5–7], but also direct practical implementations of gradiometers, gyroscopes, and inertial navigation sensors [8,9]. A second advantage as well as a challenge of atomic matter waves is that their wavelength is many orders of magnitude smaller than that of light, thus promising extremely high sensitivity, but making it difficult to implement “beamsplitters” and “mirrors” that can diffract at that scale. The highest precision can be reached through light-matter interaction [10,11], specifically the interaction of the atoms with the standing laser wave. There are different regimes in which the atoms can absorb or emit photons, imparting momentum kicks [12]. Most commonly, in the Raman regime, the change in momentum is associated with a change in the internal state of the atom [13–16], whereas in the Bragg regime, the atom remains in its internal ground state [17–21].

Here, we consider the setup of an atomic fountain interferometer (AFI) [21–24]. We focus on the Bragg regime, which allows for higher momentum space separation and is less susceptible to ac-Stark and Zeeman shifts [25]. A cloud of atoms with a well-defined initial momentum is launched into a 10 m tower [26]. After the launch, counter-propagating standing waves with appropriately controlled amplitude and phase impart momentum kicks onto the atom to implement a momentum space beamsplitter, mirror, and recombination. The scale of the atomic fountain architecture allows for time of flight on the order of seconds and thus maximizes the space-time area of the interferometer.

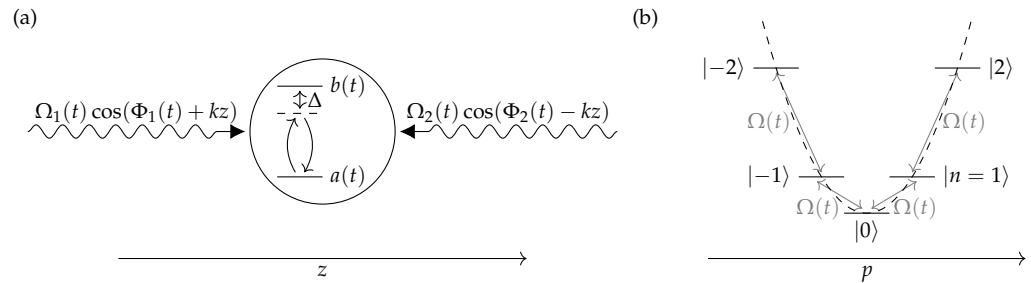


Figure 1. Interaction of an atom with interferometer laser fields in the Bragg regime. (a) Two-level atom in the coordinate representation with a two-level transition off-resonantly driven by two fields counter-propagating along the z axis, with a detuning Δ and time-dependent amplitudes $\Omega_1(t)$ and $\Omega_2(t)$ and time-dependent phases $\Phi_1(t)$ and $\Phi_2(t)$. (b) Momentum space ladder $|n\rangle$ corresponding to momentum $n \cdot 2\hbar k$, with transitions between neighboring levels being driven by the effective pulse amplitude $\Omega(t)$.

The contrast of the interferometer, particularly in the Bragg regime, is constrained by the spread in the initial momentum of the atoms [16,27] as well as deviations in the laser field intensity [28]. Here we quantify the expected contrast for different widths in the initial velocity distribution and for variations in the pulse amplitude by $\pm 10\%$ for a sequence of Rabi pulses. We further analyze the robustness of analytical pulse schemes using rapid adiabatic passage (RAP) [29,30]. These use linearly chirped laser pulses to transfer population between the momentum states. In the context of AFI, they have been demonstrated to achieve large momentum space separation [30,31]. RAP is inherently robust to deviations in the pulse amplitude. We show here that the combination of RAP and Rabi pulses significantly enhances the robustness of the full interferometric scheme.

Going beyond standard analytic schemes, modified pulse shapes have been demonstrated to improve robustness [28,32]. Finding appropriate pulse shapes is the focus of optimal control theory (OCT) [33–35]. For atom interferometers in the Raman regime and two-level dynamics, the ability of optimal control to achieve robust pulses has been demonstrated [32,36,37]. Optimal control has also been applied to Bose-Einstein condensates in atom interferometers [38]. Here, we use Krotov’s method [39–42] for an ensemble optimization [43–45] to identify robust pulses for large momentum space separation in the Bragg regime. We find that the most robust scheme overall combines optimized pulses acting only on levels $|0\rangle$ and $|1\rangle$ with analytical RAP pulses to amplify the momentum space separation.

This paper is organized as follows. In Section 2, we describe the interaction of an atom with two counter-propagating standing wave lasers inside an atomic fountain interferometer and derive its momentum space Hamiltonian in the Bragg regime. Section 3 reviews two analytic pulse schemes, first a train of Rabi pulses, and second a combination of Rabi pulses and rapid adiabatic passage are reviewed. Section 4 analyzes the robustness of these schemes in terms of the expected contrast for varying pulse amplitudes and for initial velocities of varying uncertainties. In Section 5, we describe the ensemble optimization approach used to improve the robustness of the analytical schemes. We analyze the resulting control fields and dynamics and compare the resulting robustness throughout the parameter landscape. Section 6 concludes.

2. Model

In this paper, we consider an atomic fountain interferometer [21,24,46] with light pulses in the Bragg regime [17–19]. A cloud of ultracold Rubidium atoms with atomic mass m is launched along the z axis of a ten-meter tower [26]. After the launch, the atoms are subjected

to two counter-propagating standing wave laser field waves with wave number $k = 2\pi/\lambda$ for a given laser wavelength λ . These laser fields have tunable amplitude $\Omega_1(t)$, $\Omega_2(t)$ and frequency $\Phi_1(t)$, $\Phi_2(t)$ and are used to implement momentum space “beamsplitters” and “mirrors”. A schematic of the interaction for a single atom is shown in Fig. 1 (a).

The standing-wave lasers off-resonantly drive an internal two-photon electronic transition, e.g., the Rubidium D2 line $5^2S_{1/2} \rightarrow 5^2P_{3/2}$. For a large detuning Δ the amplitude $b(z, t)$ of the excited state can be adiabatically eliminated. This results in an effective two-photon field with amplitude and phase

$$\Omega(t) = \frac{\Omega_1(t)\Omega_2(t)}{4\Delta}, \quad \varphi(t) = \Phi_1(t) - \Phi_2(t), \quad (1)$$

acting only on the ground state amplitude $a(z, t)$ [47]. A transformation from coordinate space to momentum space shows that the effective field can change the momentum only in discrete units of $2\hbar k$ relative to the rest frame defined for the initial momentum p_0 [48,49].

We thus consider the entire dynamics of the atom in momentum space, where the ground state $|0\rangle$ corresponds to the rest frame momentum p_0 and the Hilbert space is defined in terms of levels $|n\rangle$ corresponding to the momentum $p_0 + n \cdot 2\hbar k$. The Hamiltonian takes the form

$$\hat{H} = \left(\sum_{n=-\infty}^{\infty} E_n(t) |n\rangle\langle n| \right) - \left(\sum_{n=-\infty}^{\infty} (\mu \hbar \Omega(t) |n\rangle\langle n+1| + \mu \hbar \Omega^*(t) |n+1\rangle\langle n|) \right). \quad (2)$$

The time-dependent energy levels are

$$E_n(t) = n^2 \hbar \omega_k + \beta^2 \hbar \omega_k - \hbar \Omega_\Delta(t) + 2n \beta \hbar \omega_k + n \hbar \dot{\varphi}(t) \quad (3)$$

with the two-photon recoil frequency $\omega_k = 2\hbar k^2/m$, the dimensionless initial momentum $\beta = p_0/2\hbar k$, and the common light shift $\Omega_\Delta(t) = (\Omega_1^2(t) + \Omega_2^2(t))/4\Delta$. We consider here $\beta < 1$ and neglect the term proportional to β^2 . Moreover, the common light shift $\Omega_\Delta(t)$ only contributes a global phase to the dynamics of the interferometer and can be dropped. Thus, we use

$$E_n(t) \approx n^2 \hbar \omega_k + 2n \beta \hbar \omega_k + n \hbar \dot{\varphi}(t) \quad (4)$$

in the remainder of the paper.

The energy levels $E_n(t)$ form the parabolic momentum ladder shown in Fig. 1 (b). These levels are shifted by the angular frequency $\dot{\varphi}(t)$ of the driving field. An appropriate frequency can shift neighboring levels into resonance, which then allows the effective amplitude $\Omega(t)$ to transfer population. A nonzero value of β , that is, a nonzero momentum of the atom relative to the rest frame, will result in an effective detuning of this momentum space transition.

The factor μ in Eq. (2) accounts for deviations of the effective pulse amplitude $\Omega(t)$ from the optimal value, e.g., due to misalignment of the position of the atomic cloud relative to the cross section of the laser pulse. By default, we take $\mu = 1$. The effective amplitude $\Omega(t)$ is allowed to be complex-valued only in the context of optimal control, where the phase of $\Omega(t)$ expresses deviations from the frame defined by $\varphi(t)$ in Eq. (4). A complex amplitude thus allows unconstrained control of the system by tuning only $\Omega(t)$ instead of both $\Omega(t)$ and $\varphi(t)$.

For complete generality, we express the energies $E_n(t)$ and $\hbar \Omega(t)$ in units of $\hbar \omega_k$. Using the corresponding time unit of $1/\omega_k$ makes the Schrödinger equation dimensionless. For Rb-87, with a laser wavelength of $\lambda = 780$ nm, we have $\omega_k = 2\pi \cdot 15.1$ kHz, and a corresponding time unit of approximately 10^{-5} s.

3. Analytical Pulse Schemes

A full atom interferometer consists of the following steps:

1. Split the initial state $|0\rangle$ into a superposition of $|0\rangle$ and $|N\rangle$. In the example here, we will use $N = 10$ corresponding to a momentum space separation of $20 \hbar k$. This is the analogue of a beamsplitter in a classic interferometer
2. Let the atoms evolve freely as they travel up the tower. During this time, an external gravitational field or acceleration may introduce a differential phase between the state $|0\rangle$ and $|N\rangle$.
3. Swap the complex amplitudes of the $|0\rangle$ and $|N\rangle$ states. This is the analog of a mirror in a classic interferometer
4. Let the atoms continue to evolve freely as they descend the tower, potentially accumulating a further differential phase.
5. Recombine the state into a superposition of $|0\rangle$ and $|1\rangle$. In an ideal system, the population in the two output states depends on the accumulated differential phase ϕ , so that the population in $|0\rangle$ state is

$$P_0(\phi) \equiv |\langle 0 | \Psi(T) \rangle|^2 = \cos^2\left(\frac{\phi}{2}\right) \quad (5)$$

and the state $|1\rangle$ population is $P_1(\phi) = 1 - P_0(\phi)$.

The interferometer signal contrast is defined as

$$C \equiv \frac{P_{\max} - P_{\min}}{P_{\max} + P_{\min}}, \quad (6)$$

with $P_{\max} \equiv \max_{\phi} P_0(\phi) = P_0(\phi = 0)$ and $P_{\min} \equiv \min_{\phi} P_0(\phi) = P_0(\phi = \pi/2)$. In a non-ideal system, with imperfect splitting and mirror operations, population may be lost from the $|0\rangle$, $|1\rangle$ subspace at final time, and the population in the ground state may deviate from the ideal Eq. (5), resulting in a loss of contrast.

3.1. Train of Rabi pulses

A straightforward approach is to use a train of π - and $\pi/2$ -pulses to manipulate the wave function of the atoms [26,46]. Each pulse in this train uses a fixed laser frequency $\dot{\phi}(t) = \omega_L^{(n_0)}$ that is resonant with a specific transition from level n_0 to $n_0 + 1$. The transition is resonant for

$$\omega_L^{(n_0)} = -\omega_k(2n_0 + 1). \quad (7)$$

Plugging this into Eq. (4) produces ($\beta = 0$)

$$E_n^{(\text{rabi})} = (n'^2 - n')\hbar\omega_k + n_0(n_0 + 1)\hbar\omega_k, \quad (8)$$

with $n' \equiv n - n_0$. The second term contributes only a global phase and can be dropped.

Steps 1 – 5 of the full interferometer with a maximum separation of $N = 10$ are implemented by a series of Rabi pulses as shown in Fig. 2 (b). Each pulse is a Blackman shape of duration $t_{\text{rabi}} = 15 / \omega_k$, which corresponds to roughly $150 \mu\text{s}$ for Rb-87 and a laser wavelength of 780 nm. Neglecting all but the two resonant levels for each Rabi pulse allows to calculate the pulse amplitude *analytically*; The first pulse is a $\pi/2$ pulse with an amplitude chosen such that

$$\int_0^{t_{\text{rabi}}} \Omega(t) dt = \frac{\pi}{2}, \quad (9)$$

in order to produce a 50/50 superposition of $|0\rangle$ and $|1\rangle$. The pulse amplitude is $0.125 \omega_k$, corresponding to $1.88 \cdot 2\pi$ kHz.

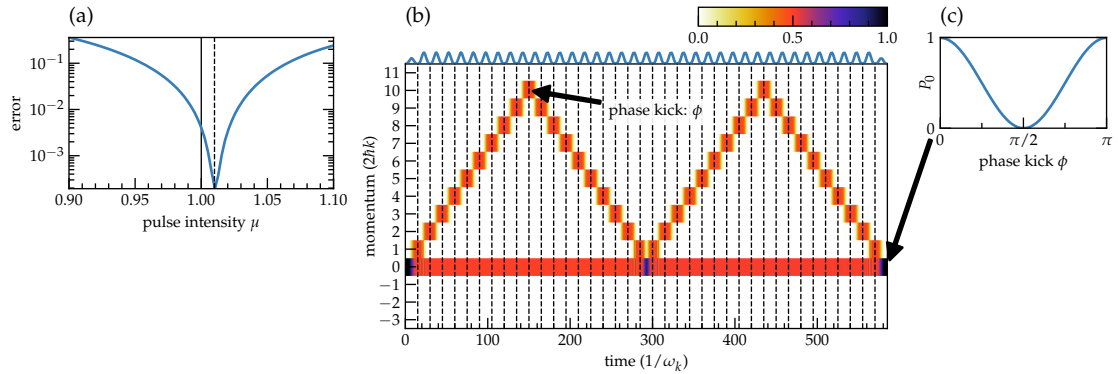


Figure 2. (a) Error $1 - |\langle 0 | \Psi(T) \rangle|^2$ of the population in the ground state after a sequence of Rabi pulses for varying pulse amplitude. The value $\mu = 1$ is the analytic value for an ideal two-level system in each transition. The minimum error is reached for $\mu \approx 1.01$, indicated by the dashed vertical line. (b) Momentum space dynamics for an interferometric scheme using a sequence of Rabi pulses. Each Rabi pulse has a Blackman shape, drawn at the top of the panel, with an amplitude adjusted by the correction determined in panel (a). The time unit $1/\omega_k$ corresponds to roughly 10^{-5} s for Rb-87 atoms and a laser wavelength of 780 nm, making the duration of the scheme (excluding the free time evolution) roughly 5.9 ms. (c) The final time population in $|0\rangle$ if an instantaneous phase kick is applied to the $|10\rangle$ component of the wave function at maximum separation.

Subsequent pulses are π -pulses at twice the amplitude of Eq. (9) that fully transfer population between neighboring levels, respectively swap the population of $|0\rangle$ and $|1\rangle$ at the center of the scheme. The final $\pi/2$ pulse recombines the population. For simplicity, we do not include the free time evolution in the scheme. The phase that would be accumulated during the free time evolution, when the interferometer is at maximum momentum separation, can be numerically emulated by applying an instantaneous phase kick to the $|10\rangle$ -component of the wave function, as indicated in Fig. 2 (b). The shown dynamics are for $\phi = 0$. A kick with a value of $\phi > 0$ only affects the population in the central SWAP pulse and at final time. The resulting final time population in $|0\rangle$ is shown in Fig. 2 (c) and matches Eq. (5).

The use of Rabi pulses is slightly complicated by the presence of the additional levels. According to Eq. (8), the transition to the next higher or lower levels is detuned by $2\omega_k$, which is not completely negligible compared to the amplitude of the π pulse, $0.25\omega_k$. The additional levels induce an effective shift in the two-level system that can be compensated with a modified pulse amplitude. In Fig. 2 (a), we numerically analyze the fidelity of the scheme depending on a scaling factor for the pulse amplitude, $\mu \neq 1$ in Eq. (2). We find that an increase in pulse amplitude by 1% results in the lowest error. Thus, we include this correction in the scheme shown in Fig. 2 (b) as well as in all future Rabi amplitudes.

3.2. Rapid adiabatic passage

An alternative formulated in Ref. [30,31] is to replace the train of pulses with a single pulse implementing rapid adiabatic passage (RAP) with a linear frequency chirp, respectively, a phase of

$$\varphi_{\text{RAP}}(t) = -\frac{\alpha\omega_k(t-t_c)^2}{2}, \quad (10)$$

where α is the (dimensionless) chirp rate and t_c is a time offset. Plugging the phase into Eq. (4) with $\beta = 0$ results in

$$E_n^{\text{RAP}}(t) = (n^2 - n\alpha(t-t_c))\hbar\omega_k. \quad (11)$$

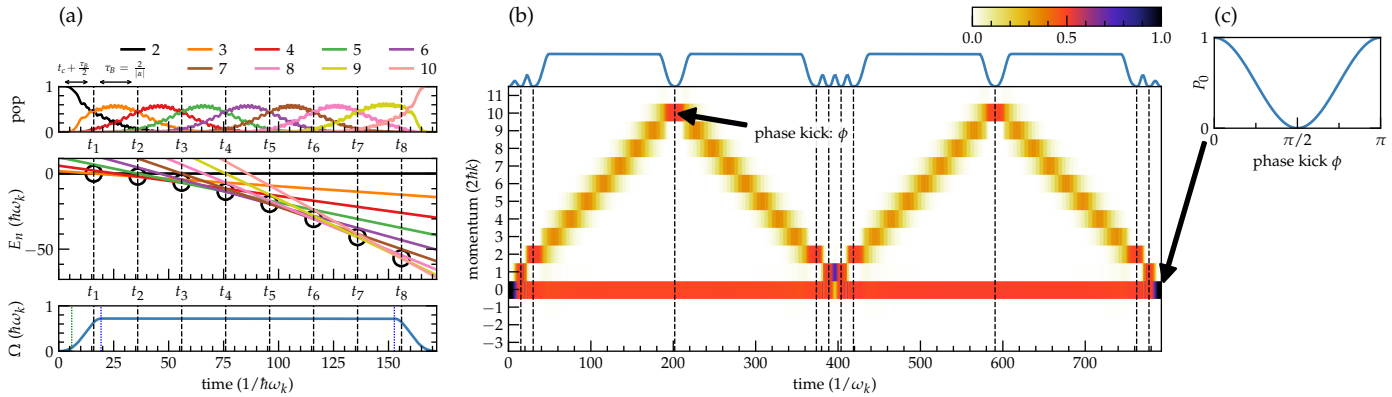


Figure 3. (a) Transfer of population from momentum state $|2\rangle$ to $|10\rangle$ using rapid adiabatic passage (RAP) with a constant linear chirp rate $\alpha = 0.1$ with an offset time of $t_c = 5.93/\omega_r$ (green dotted line, bottom). The pulse envelope $\Omega(t)$ shown in the bottom of panel (a) has a switch-on and switch-off time of $t_r = 19.25/\omega_r$ (blue dotted line), using half of a Blackman shape. The center of panel (a) shows the dynamic energy levels of the Hamiltonian according to Eq. (11). Neighboring levels cross at intervals of $\tau_B = 2/|\alpha|$, resulting in the transfer of population shown at the top of panel (a). (b) Momentum space dynamics for a full interferometric scheme using an initial $\pi/2$ and π pulse to achieve momentum space separation, cf. Fig. 2, then the RAP pulse from panel (a) to first amplify and then de-amplify the momentum space separation. The momentum components are swapped with three central π pulses. In the second half of the scheme, two additional RAP pulses amplify and de-amplify again. Finally, a π and $\pi/2$ pulse perform the recombination. The amplitudes of the envelope $\Omega(t)$ in each pulse is drawn to scale at the top of the panel. (c) The final time population in $|0\rangle$ if an instantaneous phase kick is applied to the $|10\rangle$ component of the wave function at maximum separation.

An example for the dynamic energy levels $E_n^{\text{RAP}}(t)$ and the resulting population dynamics is depicted in Fig. 3 (a), with a chirp rate $\alpha = 0.1$. Neighboring levels cross at time intervals of $\tau_B = 2/|\alpha|$, see the center of panel (a), resulting in a population transfer as shown in the top of panel (a). The offset time t_c is determined numerically together with the specific switch on / off time and the amplitude of the envelope $\Omega(t)$ shown at the bottom of panel (a). In this example, we have found $t_c = 5.927/\omega_k$ for a Blackman shape with a switch-on/off time of $19.252/\omega_k$ and a peak amplitude of $1.4\omega_k$, corresponding to roughly $21 \cdot 2\pi$ kHz for Rb-87 and a laser wavelength of 780 nm. These parameters are the result of an optimization of the transfer fidelity using the Nelder-Mead method.

A noteworthy feature of the RAP population transfer is that it is relatively insensitive to the pulse amplitude, promising some degree of robustness when used as part of an atom interferometric scheme. It also allows to go to arbitrarily high momentum states, for as long as the constant chirp can be maintained. However, it is relatively more challenging compared to the Rabi pulse scheme to use RAP for the initial splitting, the central swap of $|0\rangle$ and $|1\rangle$, or the final recombination required for the full scheme. Thus, we combine it with a small number of Rabi pulses: an initial $\pi/2$ pulse to achieve the initial splitting, followed by another π pulse to achieve sufficient separation for the RAP scheme to transfer population to maximum separation. In the center of the scheme, three π pulses swap the amplitude, and finally a π pulse and a $\pi/2$ pulse perform the recombination. The full scheme is depicted in Fig. 3 (b).

Compared to the sequence of Rabi pulses in Fig. 2 (b), the required pulse area for RAP is significantly larger; see the amplitudes shown in the top of both panels. Further compressing the RAP pulses in time would cause increasingly non-adiabatic dynamics and a breakdown of the population transfer shown in Fig. 3 (a). The fast oscillations that can be seen at the top of

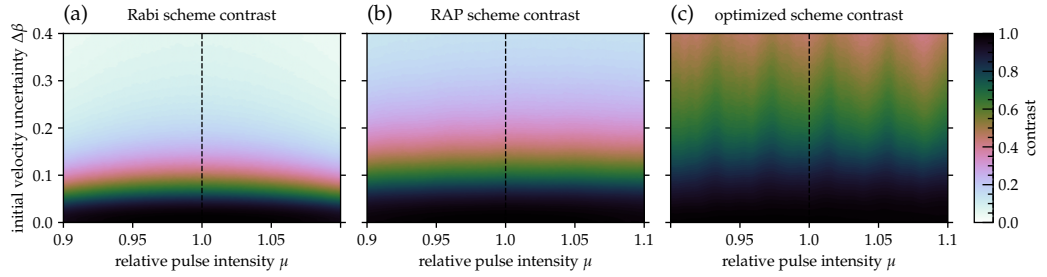


Figure 4. Contrast achieved with both analytical and optimized pulse schemes for a full $20 \hbar k$ interferometer scheme. In each panel, the expectation value of the signal contrast is shown for a fixed amplitude scaling factor μ of the ideal pulse amplitude and assuming a Gaussian distribution with width $\Delta\beta$ for the atom's initial momentum relative to the rest frame in units of $2\hbar k$. The schemes are for a train of Rabi pulses (a), a scheme using rapid adiabatic passage (b), and a scheme using optimized control pulses in combination with rapid adiabatic passage (c), cf. Figs. 2, 3, 7. The value of the contrast for each point is obtained from the average populations in the ground state, see Eq. (13).

panel (a) already are non-adiabatic effects, showing that the chosen parameters approach the time limits for RAP. Thus, the RAP scheme in Fig. 3 (b) is slightly slower than the comparable Rabi scheme in Fig. 2 (b), $T = 792.4 / \omega_k$ versus $T = 585.0 / \omega_k$. In general, this should have a negligible effect on the overall interferometer, as the free time of flight, measured in seconds [26], dominates the time for splitting, mirroring, and recombination, measured in milliseconds.

4. Robustness

The dynamics shown in Figs. 2, 3 for the analytical Rabi and RAP scheme are for ideal parameters, i.e., zero velocity relative to the rest frame and the ideal pulse amplitude, $\beta = 0$ and $\mu = 1$ in Eqs. (2, 4), where $\mu = 1$ now includes the correction of 1.01 obtained from Fig. 2 (a). We can now analyze the robustness of the different interferometric schemes with respect to variations in atom velocity and pulse amplitude. Since the width of the atomic cloud is small relative to the cross section of the laser pulse, deviations from the ideal amplitude are most likely due to the position of the atomic cloud within the laser field, or due to variations in the overall laser amplitude itself, but are the same for all atoms in ensemble. On the other hand, the velocity relative to the rest frame varies within the ensemble. It is normal-distributed with a variance that depends on the temperature of the atomic cloud.

In Fig. 4 (a, b), we show the expectation value of the contrast for static deviations from the optimal pulse amplitude by $\pm 10\%$ ($\mu \in [0.9, 1.1]$) and for β (the momentum relative to the rest frame in units of $2\hbar k$) drawn from a normal distribution with a standard deviation between 0 and 0.4. For every point in this robustness landscape, we evaluate $N = 50\,000$ samples to find

$$\begin{aligned} \bar{P}_{\max}(\mu, \Delta\beta) &= \frac{1}{N} \sum_{n=1}^N P_0(\phi = 0; \mu, \beta_n) \\ \bar{P}_{\min}(\mu, \Delta\beta) &= \frac{1}{N} \sum_{n=1}^N P_0(\phi = \frac{\pi}{2}; \mu, \beta_n), \end{aligned} \quad (12)$$

where P_0 is the population in the ground state at final time, ϕ is the differential phase accumulated between the two branches of the interferometer, and β_n is a value of β drawn from the distribution of width $\Delta\beta$. The expectation value of the contrast shown in Fig. 4 is then

$$\bar{C}(\mu, \Delta\beta) = \frac{\bar{P}_{\max}(\mu, \Delta\beta) - \bar{P}_{\min}(\mu, \Delta\beta)}{\bar{P}_{\max}(\mu, \Delta\beta) + \bar{P}_{\min}(\mu, \Delta\beta)}, \quad (13)$$

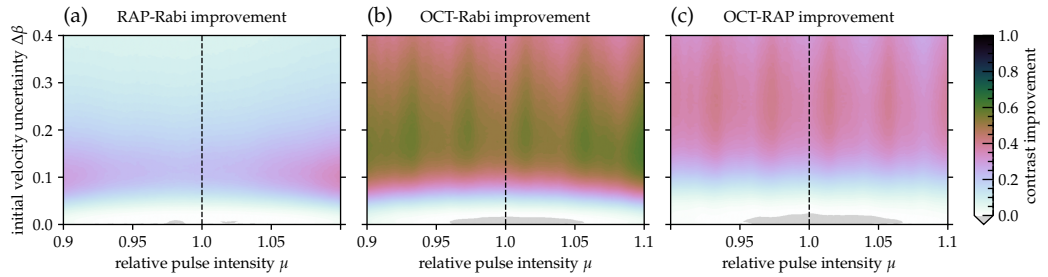


Figure 5. Contrast Improvement between different schemes. Panel (a) shows the difference between Fig. 4 (b) and Fig. 4 (a), that is, between a scheme using a train of Rabi pulses and a scheme using rapid adiabatic passage (RAP). Panels (b, c) show the difference between between Fig. 4 (c) and Fig. 4 (a), respectively Fig. 4 (c) and Fig. 4 (b); that is, between a scheme using pulses derived from optimal control theory (OCT) and the two analytic schemes (Rabi, RAP). The light gray points mark a (negligible) loss of contrast, $|\Delta C| < 0.04$ in panel (a) and $|\Delta C| < 0.01$ in panels (b, c).

cf. Eq. (6).

We find that the contrast is relatively robust with respect to deviations from the optimal pulse amplitude but decays quickly for broader distributions in the atomic velocity. Using the scheme of Rabi pulses, Fig. 2 (b), the contrast crosses the 50% mark for a standard deviation of $\Delta\beta \approx 0.1$ and approaches effectively zero for $\Delta\beta > 0.2$. Taking advantage of the rapid adiabatic passage (RAP) with the scheme shown in Fig. 3 (b), we find a measurable improvement in robustness. The sensitivity to deviations in μ nearly disappears, and the loss of contrast due to $\Delta\beta > 0$ is reduced by at least a factor of 1.5. That is, a 50% loss of contrast occurs at $\Delta\beta \approx 0.15$. Even at $\Delta\beta = 0.4$, the contrast is still $\approx 12\%$.

The change in contrast between the Rabi and RAP schemes is quantified in Fig. 5 (a). The RAP scheme improves on the Rabi scheme by an increase in contrast of up to 0.35. This maximum improvement is reached for deviations of the pulse amplitude near 10% and a standard deviation of $0.1 \cdot 2\hbar k$ in the initial momentum of the atoms in the ensemble. The light gray areas in the plot mark a loss of contrast for some point near $\Delta\beta = 0$. These losses are comparatively negligible at $|\Delta C| < 0.04$.

5. Optimal Control for Robust Pulse Schemes

To further increase the robustness, we now consider the use of optimal control theory (OCT). In general, the interferometric scheme can be split into the following steps, each of which can be optimized separately:

1. Splitting the initial state $|0\rangle$ into a superposition of $|0\rangle$ and some excited momentum state $|N_S\rangle$
2. Amplifying the superposition into a maximum momentum space separation of $|0\rangle$ and the maximum $|N\rangle$ in which the interferometer evolves freely to accumulate a differential phase. That is, transfer the momentum component $|N_S\rangle \rightarrow |N\rangle$
3. De-amplify $|N\rangle \rightarrow |N_S\rangle$
4. Swap the amplitudes of $|0\rangle$ and $|N_S\rangle$
5. Repeat the amplification and de-amplification
6. Recombine $|N_S\rangle$ and $|0\rangle$ so that the final time population in $|0\rangle$ depends on the accumulated differential phase as in Eq. (5).

For example, in the RAP scheme in Fig. 3 (b), the initial two Rabi pulses constitute the splitting step with $|N_S\rangle = |2\rangle$, the RAP pulses implement the amplification and de-amplification, the three center Rabi pulses implement a SWAP gate between the levels $|N_S = 2\rangle$ and $|0\rangle$, and the final two Rabi pulses recombine.

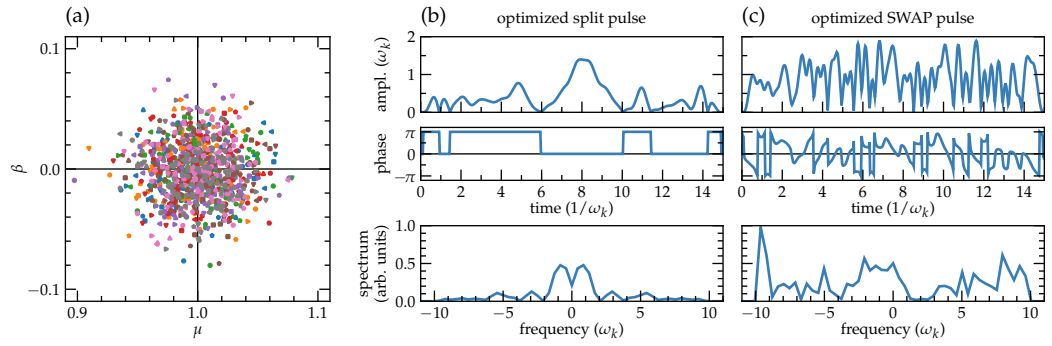


Figure 6. (a) Ensemble points used for the optimization. The sampling points are chosen from a normal distribution around $\mu = 1$ and $\beta = 0$ with a width of $\Delta\mu = \Delta\beta = 0.025$, divided into 64 batches with 16 points per batch. The different batches are distinguished by the combination of color and marker shape. (b) Optimized pulse amplitude, phase, and spectrum for the initial splitting pulse $|0\rangle \rightarrow (|0\rangle + i|1\rangle)/\sqrt{2}$. (c) Optimized pulse amplitude, phase, and spectrum for the central SWAP pulse between $|0\rangle$ and $|1\rangle$. For Rb-87 and a laser wavelength of 780 nm, the two-photon recoil frequency is $\omega_k = 2\pi \cdot 15.1$ kHz. The unit of time $1/\omega_k$ corresponds to roughly 10^{-5} s. Thus, the duration of the shown pulses is on the order of 150 μ s.

It can be shown [47] that any relative phase introduced by the amplification and de-amplification cancels out. Thus, these steps can be implemented with an optimization functional that only considers populations, e.g., for the amplification step,

$$J_{\text{pop}}(|\Psi(T)\rangle) = 1 - \frac{1}{2} \left\| \vec{P}(|\Psi(T)\rangle) - \vec{P}^{\text{tgt}} \right\|^2, \quad (14)$$

where the components of the vectors \vec{P} and \vec{P}^{tgt} are the populations in the different momentum levels for the propagated state and the target state, respectively. A relative phase introduced by the initial splitting has to be compensated in the recombination step.

The most straightforward approach is to perform the initial splitting between levels $|0\rangle$ and $|N_S\rangle = |1\rangle$ and to optimize for an effective $\pi/2$ pulse,

$$|0\rangle \rightarrow \frac{1}{\sqrt{2}}(|0\rangle + i|1\rangle), \quad |1\rangle \rightarrow \frac{1}{\sqrt{2}}(i|0\rangle + |1\rangle), \quad (15)$$

up to a global phase, i.e., using a square-modulus overlap functional [50]. This ensures that the same optimized pulse can also be used for the final recombination. For the amplification and de-amplification, we optimize starting from an RAP pulse that transfers $|1\rangle \rightarrow |10\rangle$, respectively $|10\rangle \rightarrow |1\rangle$, cf. Fig. 3 (a). The optimization modifies the envelope $\Omega(t)$ in order to minimize the population functional in Eq. (14). In principle, the chirp rate α in Eq. (10) could also be made time-dependent. Instead, we leave the chirp rate constant and allow $\Omega(t)$ to be complex-valued.

To make the optimized pulses robust with respect to deviations in the pulse amplitude and variations in the initial velocity, we employ an ensemble optimization [43–45]. That is, we consider multiple copies of the Hamiltonian, Eq. (2), each with different parameters μ and β . We then optimize over the average of the ensemble. In order to cover a large area of the parameter landscape, we consider an ensemble of 1024 points, split into 64 batches of 16 points each. Individual points are drawn randomly from a normal distribution around $\beta = 0$ and $\mu = 1$ with $\Delta\beta = \Delta\mu = 0.025$. For each batch of points, we perform an ensemble optimization with Krotov's method [39–42,47] for 1000 iterations before moving to the next batch. The procedure continues to loop around the batches until convergence is reached, that is, there is

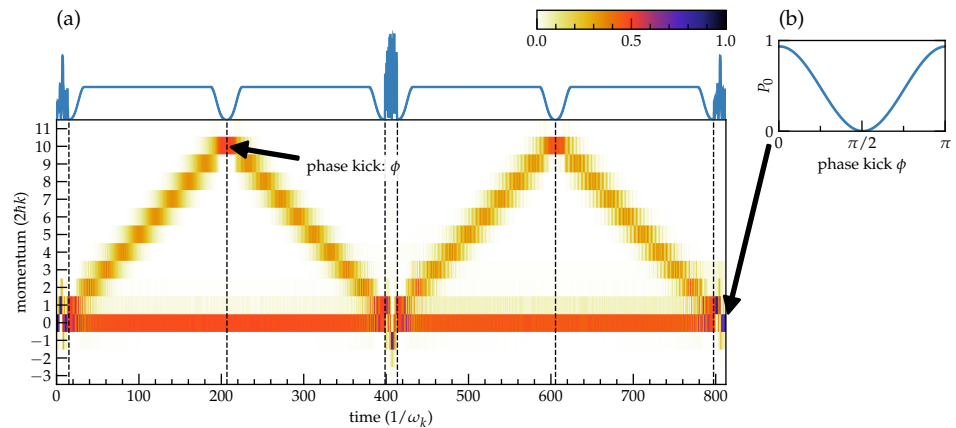


Figure 7. (a) Momentum space dynamics for interferometric scheme using optimized pulses in combination with rapid adiabatic passage (RAP). The optimized pulses are those shown in Fig. 6 (b, c) and implement the initial splitting, the center SWAP, and the final recombination between levels $|0\rangle$ and $|1\rangle$. These are combined with RAP pulses similar to the one shown in Fig. 3 (a) transferring population between $|1\rangle$ and $|10\rangle$. All pulse amplitudes are shown to scale at the top of the panel. (b) The final time population in $|0\rangle$ if an instantaneous phase kick is applied to the $|10\rangle$ component of the wave function at maximum separation. The maximum population at $\phi = 0$ or $\phi = \pi$ is 0.934 and the minimum population at $\phi = \frac{\pi}{2}$ is 0.001.

no significant improvement in the fidelity reachable within 1000 iterations compared to the previous batch.

The sampling points μ and β for the different batches are shown in Fig. 6 (a). We find the chosen width of the sampling point distribution $\Delta\beta = \Delta\mu = 0.025$ to be the maximum width for which an average fidelity on the order of 10^{-3} is achievable for the individual components of the interferometer.

As we want to explore the limits of robustness achievable via optimal control, we do not restrict the optimized control fields to amplitudes or spectral widths that are easily obtained with current experimental setups. At the same time, we would like to avoid entirely unrealistic parameter regimes. Thus, we place a bound on the pulse amplitude at $\Omega_{\max} = 1.5\omega_k$, roughly an order of magnitude higher than the typical amplitude required for a π Rabi pulse, and roughly twice the amplitude of the RAP pulses used for the momentum transfer. Similarly, the spectral width is limited to $10\omega_k$. Both the amplitude and the spectral width are well within an order of magnitude of the current capabilities of the atomic fountain experimental setup.

The resulting pulses for the initial splitting (an effective $\pi/2$ pulse), and for the SWAP gate are shown in Fig. 6 (b, c). The effective $\pi/2$ pulse is a relatively simple pulse shape. In particular, it does not require a time-dependent phase, i.e., the imaginary part of the control field $\Omega(t)$. The SWAP gate is more difficult to realize, and saturates the amplitude and spectral limits placed on the control that allow to reach the almost perfect gate fidelity.

For the optimization of the RAP pulse that amplifies and de-amplifies the momentum space separation, we find that the optimization only adds negligible corrections to the pulse shape. This is a testament to the inherent robustness of rapid adiabatic passage. In fact, when combining the optimized components of the interferometer into a full scheme and analyzing the resulting robustness, we see no clear advantage in using the RAP pulses with an optimized amplitude. Thus, the full “optimized” pulse scheme uses the pulse shown in Fig. 6 (b) as the initial and final component, and the pulse in Fig. 6 (c) as the center SWAP, but analytical RAP pulses otherwise.

The full optimized scheme and the resulting dynamics in the ideal case ($\mu = 1, \beta = 0$) are shown in Fig. 7. We can see that there are visible deviations from the simple analytic schemes in Figs. 2, 3. In particular, the optimized splitting and SWAP pulses populate outside the two-level subspace $|0\rangle, |1\rangle$, at intermediary times. The final time population in $|0\rangle$ differs measurably from the analytical schemes, reaching 0.93 in Fig. 7 (c). However, since the population for a differential phase of $\phi = \pi$ is still 0.001, this does not affect *contrast*, which is still ≈ 1 according to Eq. (6).

The contrast of the full scheme for values of $\mu \neq 1$ and for an initial momentum drawn from a normal distribution with $\Delta\beta > 0$ is shown in Fig. 4 (c). We observe a considerable improvement. The limit for 50% contrast is pushed well beyond $\Delta\beta = 0.3$. Even for $\Delta\beta = 0.4$, the minimum contrast is still 41% or higher. Remarkably, the enhancement in robustness extends far beyond the value of $\Delta\beta = 0.025$ that was used in the ensemble optimization. The improvement relative to the fully analytical Rabi and RAP schemes is shown in Fig 5 (b, c). Within the explored parameter regime, the maximum absolute improvement in contrast is 0.61 and 0.41, respectively. The losses marked in light gray are $|\Delta C| < 0.01$ in both cases.

6. Conclusion and Outlook

We have numerically analyzed the expected robustness of several complete schemes for an atomic fountain interferometer reaching a momentum space separation of $20\hbar k$. For purely analytic schemes, we find that robustness can be increased considerably by using rapid adiabatic passage to transfer population after the initial separation. This comes at the cost of an increase in pulse area, reaching about the limit of current experimental capabilities. However, the use of rapid adiabatic passage fundamentally allows to achieve arbitrarily high momentum space separation and preserving very high robustness, as long as the linear chirp of the laser frequency can be maintained. In fact, we do not find that the robustness of the RAP pulses can be substantially improved by optimal control. In contrast, optimal control theory can significantly improve the initial splitting and swapping of amplitudes in the middle of the interferometric scheme. Again, this comes at the cost of an increase in pulse area. The optimized pulses presented here are on the border of current experimental capabilities in terms of pulse amplitude and spectral width, but well within an order of magnitude. Thus, we expect these pulses to be realizable in the future.

Combining optimized pulses with rapid adiabatic passage into a full scheme results in a very robust scheme if the uncertainty of the initial momentum of the atoms in the interferometer is $> 0.1 \cdot 2\hbar k$. Even for relatively large uncertainties of $0.4 \cdot 2\hbar k$ or higher, a contrast of 40% is maintained. Due to the combination with analytic RAP pulses, we expect this contrast to be maintained even for much higher momentum space separation.

The optimized scheme identified here opens several avenues for future exploration. For implementation in the lab, the pulse area and spectral width of the optimized pulses would have to be reduced by at least a factor of three. As the goal here was to identify maximally robust pulses without stringent constraints, the limits of robustness within currently achievable constraints of a specific experimental setup have not been fully probed. As RAP was identified here as a core component of a robust scheme with large momentum space separation, it would be worthwhile to consider the combination of RAP with other two-level control schemes such as those derived from nuclear magnetic resonance [51].

We have assumed here that the deviations in the pulse amplitude are homogeneous, i.e., the atomic cloud is small relative to the cross section of the laser. Further, we have assumed that there are no time-dependent fluctuations in the laser for the duration of the pulse scheme, on the order of milliseconds. Strategies for mitigating time-dependent noise will be considered in future work. Spatial distortions in the laser profile could be taken into account by extending the model beyond plane waves [52].

More generally, the sensitivity of the interferometer could be enhanced by exploiting correlation between the atoms, e.g., spin squeezing [53,54]. We have applied optimal control to the creation of such squeezed states [55]. Going forward, we would like to explore the use of optimal control to further enhance the robustness of correlated atoms in atom interferometric schemes, including alternative realizations such as tractor atom interferometers [56].

Acknowledgments

The authors thank Mark Kasevich, Remy Notermans, Chris Overstreet, Peter Asenbaum, Tim Kovachy, and Sebastián Carrasco for fruitful discussions. This work was partially supported by ECI-DIRA program at the DEVCOM Army Research Laboratory. MHG acknowledges support by the DEVCOM Army Research Laboratory under Cooperative Agreement Number W911NF-16-2-0147.

References

1. Berman, P.R., Ed. *Atom Interferometry*; Academic Press: San Diego, CA, 1997. <https://doi.org/10.1016/b978-0-12-092460-8.x5000-0>.
2. Baudon, J.; Mathevet, R.; Robert, J. Atomic interferometry. *J. Phys. B* **1999**, *32*, R173. <https://doi.org/10.1088/0953-4075/32/15/201>.
3. Cronin, A.D.; Schmiedmayer, J.; Pritchard, D.E. Optics and interferometry with atoms and molecules. *Rev. Mod. Phys.* **2009**, *81*, 1051. <https://doi.org/10.1103/revmodphys.81.1051>.
4. Degen, C.L.; Reinhard, F.; Cappellaro, P. Quantum sensing. *Rev. Mod. Phys.* **2017**, *89*, 035002. <https://doi.org/10.1103/RevModPhys.89.035002>.
5. Dimopoulos, S.; Graham, P.W.; Hogan, J.M.; Kasevich, M.A. General relativistic effects in atom interferometry. *Phys. Rev. D* **2008**, *78*, 042003. <https://doi.org/10.1103/physrevd.78.042003>.
6. Dimopoulos, S.; Graham, P.W.; Hogan, J.M.; Kasevich, M.A.; Rajendran, S. Atomic gravitational wave interferometric sensor. *Phys. Rev. D* **2008**, *78*, 122002. <https://doi.org/10.1103/physrevd.78.122002>.
7. Schlippert, D.; Hartwig, J.; Albers, H.; Richardson, L.; Schubert, C.; Roura, A.; Schleich, W.; Ertmer, W.; Rasel, E. Quantum Test of the Universality of Free Fall. *Phys. Rev. Lett.* **2014**, *112*, 203002. <https://doi.org/10.1103/physrevlett.112.203002>.
8. Abe, M.; Adamson, P.; Borcean, M.; Bortoletto, D.; Bridges, K.; Carman, S.P.; Chattopadhyay, S.; Coleman, J.; Curfman, N.M.; DeRose, K.; et al. Matter-wave Atomic Gradiometer Interferometric Sensor (MAGIS-100). *Quantum Sci. Technol.* **2021**, *6*, 044003. <https://doi.org/10.1088/2058-9565/abf719>.
9. Narducci, F.A.; Black, A.T.; Burke, J.H. Advances toward fieldable atom interferometers. *Adv. Phys. X* **2022**, *7*. <https://doi.org/10.1080/23746149.2021.1946426>.
10. Shore, B.W. *Manipulating Quantum Structures Using Laser Pulses*; Cambridge University Press, 2011.
11. Berman, P.R.; Malinovsky, V.S. *Principles of Laser Spectroscopy and Quantum Optics*; Princeton University Press, 2011.
12. Hartmann, S.; Jenewein, J.; Giese, E.; Abend, S.; Roura, A.; Rasel, E.M.; Schleich, W.P. Regimes of atomic diffraction: Raman versus Bragg diffraction in retroreflective geometries. *Phys. Rev. A* **2020**, *101*, 053610. <https://doi.org/10.1103/physreva.101.053610>.
13. Bordé, C. Atomic interferometry with internal state labelling. *Phys. Lett. A* **1989**, *140*, 10. [https://doi.org/10.1016/0375-9601\(89\)90537-9](https://doi.org/10.1016/0375-9601(89)90537-9).
14. Kasevich, M.; Chu, S. Atomic interferometry using stimulated Raman transitions. *Phys. Rev. Lett.* **1991**, *67*, 181. <https://doi.org/10.1103/physrevlett.67.181>.
15. Kasevich, M.; Chu, S. Measurement of the gravitational acceleration of an atom with a light-pulse atom interferometer. *Appl. Phys. B* **1992**, *54*, 321. <https://doi.org/10.1007/bf00325375>.
16. McGuirk, J.M.; Snadden, M.J.; Kasevich, M.A. Large Area Light-Pulse Atom Interferometry. *Phys. Rev. Lett.* **2000**, *85*, 4498. <https://doi.org/10.1103/physrevlett.85.4498>.
17. Chebotayev, V.P.; Kasantsev, A.P.; Yakovlev, V.P.; Dubetsky, B.Y. Interference of atoms in separated optical fields. *J. Opt. Soc. Am. B* **1985**, *2*, 1791. <https://doi.org/10.1364/josab.2.001791>.
18. Giltner, D.M.; McGowan, R.W.; Lee, S.A. Atom Interferometer Based on Bragg Scattering from Standing Light Waves. *Phys. Rev. Lett.* **1995**, *75*, 2638. <https://doi.org/10.1103/physrevlett.75.2638>.

19. Rasel, E.M.; Oberthaler, M.K.; Batelaan, H.; Schmiedmayer, J.; Zeilinger, A. Atom Wave Interferometry with Diffraction Gratings of Light. *Phys. Rev. Lett.* **1995**, *75*, 2633. <https://doi.org/10.1103/physrevlett.75.2633>.
20. Delhuille, R.; Champenois, C.; Büchner, M.; Jozefowski, L.; Rizzo, C.; Tréneç, G.; Vigué, J. High-contrast Mach–Zehnder lithium-atom interferometer in the Bragg regime. *Appl. Phys. B* **2002**, *74*, 489. <https://doi.org/10.1007/s003400200840>.
21. Müller, H.; Chiow, S.w.; Long, Q.; Herrmann, S.; Chu, S. Atom Interferometry with up to 24-Photon-Momentum-Transfer Beam Splitters. *Phys. Rev. Lett.* **2008**, *100*, 180405. <https://doi.org/10.1103/physrevlett.100.180405>.
22. Marchi, A.d. The Optically Pumped Caesium Fountain: 10^{-15} Frequency Accuracy? *Metrologia* **1982**, *18*, 103. <https://doi.org/10.1088/0026-1394/18/3/002>.
23. Kasevich, M.A.; Riis, E.; Chu, S.; DeVoe, R.G. Atomic fountains and clocks. *Optics News* **1989**, *15*, 31. <https://doi.org/10.1364/on.15.12.000031>.
24. Kasevich, M.A.; Riis, E.; Chu, S.; DeVoe, R.G. rf spectroscopy in an atomic fountain. *Phys. Rev. Lett.* **1989**, *63*, 612. <https://doi.org/10.1103/physrevlett.63.612>.
25. Altin, P.A.; Johnsson, M.T.; Negnevitsky, V.; Dennis, G.R.; Anderson, R.P.; Debs, J.E.; Szigeti, S.S.; Hardman, K.S.; Bennetts, S.; McDonald, G.D.; et al. Precision atomic gravimeter based on Bragg diffraction. *New J. Phys.* **2013**, *15*, 023009. <https://doi.org/10.1088/1367-2630/15/2/023009>.
26. Kovachy, T.; Asenbaum, P.; Overstreet, C.; Donnelly, C.A.; Dickerson, S.M.; Sugarbaker, A.; Hogan, J.M.; Kasevich, M.A. Quantum superposition at the half-metre scale. *Nature* **2015**, *528*, 530. <https://doi.org/10.1038/nature16155>.
27. Szigeti, S.S.; Debs, J.E.; Hope, J.J.; Robins, N.P.; Close, J.D. Why momentum width matters for atom interferometry with Bragg pulses. *New J. Phys.* **2012**, *14*, 023009. <https://doi.org/10.1088/1367-2630/14/2/023009>.
28. Luo, Y.; Yan, S.; Hu, Q.; Jia, A.; Wei, C.; Yang, J. Contrast enhancement via shaped Raman pulses for thermal cold atom cloud interferometry. *Eur. Phys. J. D* **2016**, *70*, 262. <https://doi.org/10.1140/epjd/e2016-70428-6>.
29. Peik, E.; Ben Dahan, M.; Bouchoule, I.; Castin, Y.; Salomon, C. Bloch oscillations of atoms, adiabatic rapid passage, and monokinetic atomic beams. *Phys. Rev. A* **1997**, *55*, 2989. <https://doi.org/10.1103/physreva.55.2989>.
30. Malinovsky, V.S.; Berman, P.R. Momentum transfer using chirped standing-wave fields: Bragg scattering. *Phys. Rev. A* **2003**, *68*, 023610. <https://doi.org/10.1103/physreva.68.023610>.
31. Kovachy, T.; Chiow, S.w.; Kasevich, M.A. Adiabatic-rapid-passage multiphoton Bragg atom optics. *Phys. Rev. A* **2012**, *86*, 011606. <https://doi.org/10.1103/PhysRevA.86.011606>.
32. Saywell, J.C.; Kuprov, I.; Goodwin, D.; Carey, M.; Freegarde, T. Optimal control of mirror pulses for cold-atom interferometry. *Phys. Rev. A* **2018**, *98*, 023625. <https://doi.org/10.1103/physreva.98.023625>.
33. Brumer, P.; Shapiro, M. *Principles and Applications of the Quantum Control of Molecular Processes*; Wiley Interscience, 2003.
34. Brif, C.; Chakrabarti, R.; Rabitz, H. Control of quantum phenomena: past, present and future. *New J. Phys.* **2010**, *12*, 075008.
35. Sola, I.R.; Chang, B.Y.; Malinovskaya, S.A.; Malinovsky, V.S. Quantum Control in Multilevel Systems. In *Advances In Atomic, Molecular, and Optical Physics*; Arimondo, E.; DiMauro, L.F.; Yelin, S.F., Eds.; Academic Press, 2018; Vol. 67, pp. 151–256. <https://doi.org/https://doi.org/10.1016/bs.aamop.2018.02.003>.
36. Saywell, J.C.; Carey, M.; Belal, M.; Kuprov, I.; Freegarde, T. Optimal control of Raman pulse sequences for atom interferometry. *J. Phys. B* **2020**, *53*, 085006. <https://doi.org/10.1088/1361-6455/ab6df6>.
37. Saywell, J.C.; Carey, M.; Kuprov, I.; Freegarde, T. Biselective pulses for large-area atom interferometry. *Phys. Rev. A* **2020**, *101*, 063625. <https://doi.org/10.1103/physreva.101.063625>.
38. van Frank, S.; Negretti, A.; Berrada, T.; Bücker, R.; Montangero, S.; Schaff, J.F.; Schumm, T.; Calarco, T.; Schmiedmayer, J. Interferometry with non-classical motional states of a Bose–Einstein condensate. *Nat. Commun.* **2014**, *5*, 4009. <https://doi.org/10.1038/ncomms5009>.

39. Tannor, D.J.; Kazakov, V.; Orlov, V. Control of Photochemical Branching: Novel Procedures for Finding Optimal Pulses and Global Upper Bounds. In *Time-Dependent Quantum Molecular Dynamics*; Springer US, 1992; pp. 347–360.
40. Somló, J.; Kazakov, V.A.; Tannor, D.J. Controlled dissociation of I₂ via optical transitions between the X and B electronic states. *Chem. Phys.* **1993**, *172*, 85. [https://doi.org/10.1016/0301-0104\(93\)80108-L](https://doi.org/10.1016/0301-0104(93)80108-L).
41. Reich, D.M.; Ndong, M.; Koch, C.P. Monotonically convergent optimization in quantum control using Krotov's method. *J. Chem. Phys.* **2012**, *136*, 104103. <https://doi.org/10.1063/1.3691827>.
42. Goerz, M.H.; Basilewitsch, D.; Gago-Encinas, F.; Krauss, M.G.; Horn, K.P.; Reich, D.M.; Koch, C.P. Krotov: A Python implementation of Krotov's method for quantum optimal control. *SciPost Phys.* **2019**, *7*, 080. <https://doi.org/10.21468/scipostphys.7.6.080>.
43. Li, J.S.; Khaneja, N. Ensemble Control of Bloch Equations. *IEEE Trans. Automat. Contr.* **2009**, *54*, 528. <https://doi.org/10.1109/tac.2009.2012983>.
44. Chen, C.; Dong, D.; Long, R.; Petersen, I.R.; Rabitz, H.A. Sampling-based learning control of inhomogeneous quantum ensembles. *Phys. Rev. A* **2014**, *89*, 023402. <https://doi.org/10.1103/physreva.89.023402>.
45. Goerz, M.H.; Halperin, E.J.; Aytac, J.M.; Koch, C.P.; Whaley, K.B. Robustness of high-fidelity Rydberg gates with single-site addressability. *Phys. Rev. A* **2014**, *90*, 032329. <https://doi.org/10.1103/PhysRevA.90.032329>.
46. Chiow, S.w.; Kovachy, T.; Chien, H.C.; Kasevich, M.A. 102 ħk large area atom interferometers. *Phys. Rev. Lett.* **2011**, *107*, 130403. <https://doi.org/10.1103/PhysRevLett.107.130403>.
47. Goerz, M.H.; Kasevich, M.A.; Malinovsky, V.S. Quantum optimal control for atomic fountain interferometry. In Proceedings of the Proc. SPIE 11700, Optical and Quantum Sensing and Precision Metrology, 2021. <https://doi.org/10.1117/12.2587002>.
48. Wicht, A.; Sarajlic, E.; Hensley, J.M.; Chu, S. Phase shifts in precision atom interferometry due to the localization of atoms and optical fields. *Phys. Rev. A* **2005**, *72*, 023602. <https://doi.org/10.1103/physreva.72.023602>.
49. Kovachy, T.; Hogan, J.M.; Johnson, D.M.S.; Kasevich, M.A. Optical lattices as waveguides and beam splitters for atom interferometry: An analytical treatment and proposal of applications. *Phys. Rev. A* **2010**, *82*, 013638. <https://doi.org/10.1103/physreva.82.013638>.
50. Palao, J.P.; Kosloff, R. Optimal control theory for unitary transformations. *Phys. Rev. A* **2003**, *68*, 062308. <https://doi.org/10.1103/PhysRevA.68.062308>.
51. Dunning, A.; Gregory, R.; Bateman, J.; Cooper, N.; Himsworth, M.; Jones, J.A.; Freegarde, T. Composite pulses for interferometry in a thermal cold atom cloud. *Phys. Rev. A* **2014**, *90*, 033608. <https://doi.org/10.1103/physreva.90.033608>.
52. Fitzek, F.; Siemś, J.N.; Seckmeyer, S.; Ahlers, H.; Rasel, E.M.; Hammerer, K.; Gaaloul, N. Universal atom interferometer simulation of elastic scattering processes. *Sci. Rep.* **2020**, *10*, 22120. <https://doi.org/10.1038/s41598-020-78859-1>.
53. Pezzè, L.; Smerzi, A.; Oberthaler, M.K.; Schmied, R.; Treutlein, P. Quantum metrology with nonclassical states of atomic ensembles. *Rev. Mod. Phys.* **2018**, *90*, 035005. <https://doi.org/10.1103/RevModPhys.90.035005>.
54. Brif, C.; Ruzic, B.P.; Biedermann, G.W. Characterization of Errors in Interferometry with Entangled Atoms. *PRX Quantum* **2020**, *1*, 010306. <https://doi.org/10.1103/prxquantum.1.010306>.
55. Carrasco, S.C.; Goerz, M.H.; Li, Z.; Colombo, S.; Vuletić, V.; Malinovsky, V.S. Extreme Spin Squeezing via Optimized One-Axis Twisting and Rotations. *Phys. Rev. Applied* **2022**, *17*, 064050. <https://doi.org/10.1103/physrevapplied.17.064050>.
56. Raitzel, G.; Duspayev, A.; Dash, B.; Carrasco, S.C.; Goerz, M.H.; Vuletić, V.; Malinovsky, V.S. Principles of tractor atom interferometry. *Quantum Sci. Technol.* **2022**, *8*, 014001. <https://doi.org/10.1088/2058-9565/ac9429>.